



High-speed silicon Michelson interferometer modulator and streamlined IMDD PAM-4 transmission of Mach-Zehnder modulators for the 2 μm wavelength band

WEI CAO,¹  SHENGAO LIU,¹ CALLUM G. LITTLEJOHNS,¹ DAVID J. THOMSON,¹ MILOS NEDELJKOVIC,¹  WEIWEI ZHANG,¹  KE LI,¹  MEHDI BANAKAR,¹ YING TRAN,¹ XINGZHAO YAN,¹ HAN DU,¹  ZHENGQI REN,¹ FREDERIC GARDES,¹  GRAHAM T. REED,¹ AND GORAN Z. MASHANOVICH^{1,2,*}

¹*Optoelectronics Research Centre, University of Southampton, University Road, Southampton, Hampshire SO17 1BJ, United Kingdom*

²*School of Electrical Engineering, University of Belgrade, 11120 Belgrade, Serbia*

**g.mashanovich@soton.ac.uk*

Abstract: We demonstrate high-speed silicon modulators optimized for operating at the wavelength of 2 μm . The Mach-Zehnder interferometer (MZI) carrier-depletion modulator with 2 mm phase shifter has a single-arm modulation efficiency ($V_{\pi} \cdot L_{\pi}$) of 2.89 V·cm at 4 V reverse bias. Using a push-pull configuration it operates at a data rate of 25 Gbit/s OOK with an extinction ratio of 6.25 dB. We also proposed a mathematically-analysed streamlined IMDD PAM-4 scheme and successfully demonstrated a 25 Gbit/s datarate PAM-4 with the same 2 mm modulator. A Michelson interferometer carrier-depletion modulator with 0.5 mm phase shift length has also been shown with modulation efficiency ($V_{\pi} \cdot L_{\pi}$) of 1.36 V·cm at 4 V reverse bias and data rate of 20 Gbit/s OOK. The Michelson interferometer modulator performs similarly to a Mach-Zehnder modulator with twice the phase shifter length.

Published by The Optical Society under the terms of the [Creative Commons Attribution 4.0 License](https://creativecommons.org/licenses/by/4.0/). Further distribution of this work must maintain attribution to the author(s) and the published article's title, journal citation, and DOI.

1. Introduction

Rapidly growing internet demand has stimulated innovations in fibre based communications system such as erbium doped fibre amplifiers (EDFA), wavelength division multiplexing (WDM) and high-spectral efficiency coding [1]. With the digital signal processing (DSP) assisted coherent detector, we are about to touch the capacity limit of conventional single core single mode fibres (SMFs) [2,3]. To further keep up with demand and to bust the “capacity crunch”, industry has recently settled on adopting spatial division multiplexing (SDM) as an imminent next step; that is to use multi-core and multiple parallel fibres to further scale up the capacity. Massive fibre parallelism however may face diminishing return eventually and the associated scaled-up power consumption can be another complication. If only we could replicate the success of the EDFA and WDM by developing technologies to further increase spectral efficiency without a significant increase in power consumption. Such technologies when used in conjunction with SDM, would be able to sustain a capacity boost in the long run.

One possible route is to enhance the fundamental property of the optical fibre and hence increase the Non-Linear Shannon Limit. An emerging candidate is hollow-core photonic bandgap fibre (HC-PBGF), creating bandgaps through an engineered wavelength-sized cladding structure, which traps the majority portion of the optical mode inside an air core. Air has orders of

magnitude lower Rayleigh scattering and has an infrared absorption edge at a significantly longer wavelength. The loss in hollow core fibre is hence dominated by surface scattering and the optimal low-loss window has shifted to an optical wavelength around $2 \mu\text{m}$. It could theoretically reach around 0.1 dB/km for a 19c-sized air core fibre [4,5], compares favourably to the 0.2 dB/km-loss of SMF fibre that is widely used currently. Furthermore, due to the air core, hollow-core fibre exhibits exceptionally low nonlinearity. This means it can sustain a much higher launch power, hence gaining a higher optical signal to noise ratio (OSNR) and a higher spectral efficiency. Other merits of hollow-core fibre include lower latency [6], dispersion control [7], high thermal stability [8] and high radiation hardness [9].

Wavelengths around $2 \mu\text{m}$ coincides well with the gain windows of thulium ions. Thus thulium-doped fibre amplifiers (TDFA) can be used as a counterpart of the EDFA in the C-band. Furthermore, the Silicon-on-Insulator (SOI) platform with a 220 nm Si top layer is compatible with a $2 \mu\text{m}$ wavelength. This makes the $2 \mu\text{m}$ wavelength CMOS fabrication compatible and large scale integration become viable. The triumvirate of hollow-core fibre, TDFA and silicon photonics can therefore enable a new telecommunication window at $2 \mu\text{m}$.

Silicon based defect detector has shown to operate at 20 Gbit/s at $2 \mu\text{m}$ [10]. Recently there are exciting breakthroughs in silicon based $2 \mu\text{m}$ modulators, with 12.5 Gbit/s OOK MZM [11], 20 Gbit/s OOK MZM [12], 50 Gbit/s OOK MZM (post-FEC) [13], and 12.5 Gbit/s OOK ring [14]. In this work, we explore and demonstrate high-speed PAM-4 operation and Michelson interferometer modulators both at $2 \mu\text{m}$ wavelength. Compared to some previous works, the devices showed low insertion loss, high extinction ratio and is FEC or DSP free.

2. Design and fabrication

The plasma dispersion effect in silicon has been widely used in C-band and O-band high-speed silicon modulators. As shown in Fig. 1, light at a $2 \mu\text{m}$ wavelength has a stronger interaction with both electrons and holes than at 1550 nm [15], resulting a higher refractive index change. The modulator in our design uses a reverse biased PN junction as its phase shifter, and is optimized for operating at a $2 \mu\text{m}$ wavelength. The optimization is carried out in a series of simulations using both Silvaco TCAD for electrical analysis and MATLAB [16] for the optical mode calculation.

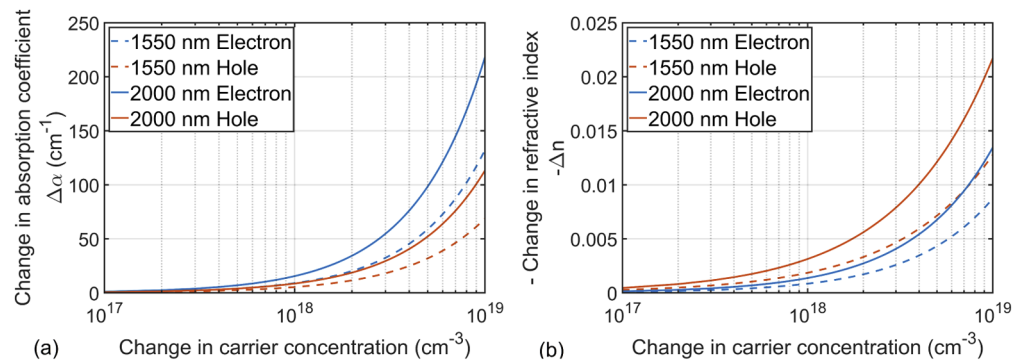


Fig. 1. Plasma dispersion effect in silicon at 1550 nm and 2000 nm wavelength, predicted by the semi-empirical equations [15]. (a) The refractive index change against change in carrier concentrations. (b) The absorption coefficient change against change in carrier concentrations.

The phase shifter exploits the carrier depletion effect, and as shown in Fig. 2(a) it comprises a PN junction. The device is fabricated in a CORNERSTONE multi-project wafer (MPW) run [17]. The active run uses 220 nm SOI wafers with a $2 \mu\text{m}$ buried oxide (BOX) layer. The silicon rib waveguide is 550 nm wide and etched to a thickness of 100 nm in the slab region. The top

silicon dioxide cladding layer is at least $1 \mu\text{m}$ thick, which is sufficiently thick to contain the swelled optical mode of $2 \mu\text{m}$ and minimize the mode overlap with the metal electrodes on top of the waveguides.

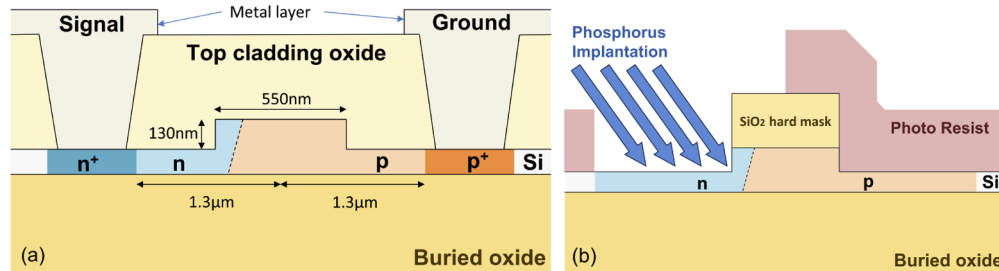


Fig. 2. (a) The phase shifter cross section of the $2 \mu\text{m}$ MZI modulator. (b) Self-aligned process used in CORNERSTONE MPW.

The n-type doping is implanted through a self-aligned mask so that the junction appears angled and positioned towards the n side. In the self-alignment process, depicted in Fig. 2(b), a silica hard mask was used to etch the rib waveguide and also as a mask for the phosphorous implantation. The photo resist edge can then be placed anywhere within the rib width and the PN junction position will be independent of the resist edge. In order for the n-type dopant to penetrate enough into the waveguide, the implantation is performed at an angle of 45 degrees and without any rotation. The self-alignment step helps reduce the junction position variation across devices introduced by the lithography [18]. The target doping concentrations in the simulation are $3.8 \times 10^{17} \text{ cm}^{-3}$, $1.1 \times 10^{18} \text{ cm}^{-3}$, $1.5 \times 10^{17} \text{ cm}^{-3}$, $7.5 \times 10^{17} \text{ cm}^{-3}$, $1 \times 10^{20} \text{ cm}^{-3}$ and $1 \times 10^{20} \text{ cm}^{-3}$ for the p, n, p (rib), n (rib), p+, and n+ regions respectively. The higher n to p-type doping ratio helps the depletion region expands into the p-type doped side. The highly doped region separation is defined by the distance between the inner edge of the highly doped region and the waveguide centre. According to the Fig. 3, the simulated junction bandwidth improves when such the separation distance is small. But the optical mode will strongly interact with the free carriers if the highly doped region is too close to the waveguide, resulting a large optical loss. Due to the annealing step performed after the implantation, the actual doping profile will be a gradual transition; this has been taken account for in the simulation. In this work, the highly doped regions are $1.3 \mu\text{m}$ away from the waveguide centre.

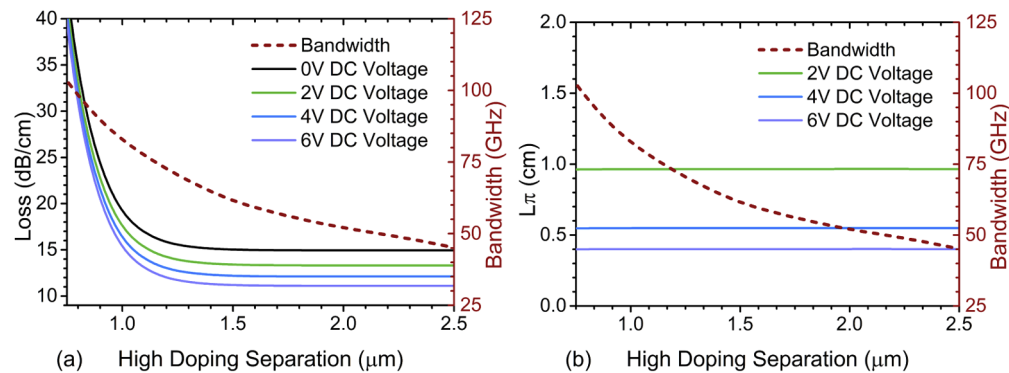


Fig. 3. MZI modulator phase shifter simulation of variation in highly doped region separation at 1950 nm wavelength. (a) Simulated loss. (b) Simulated L_{π} .

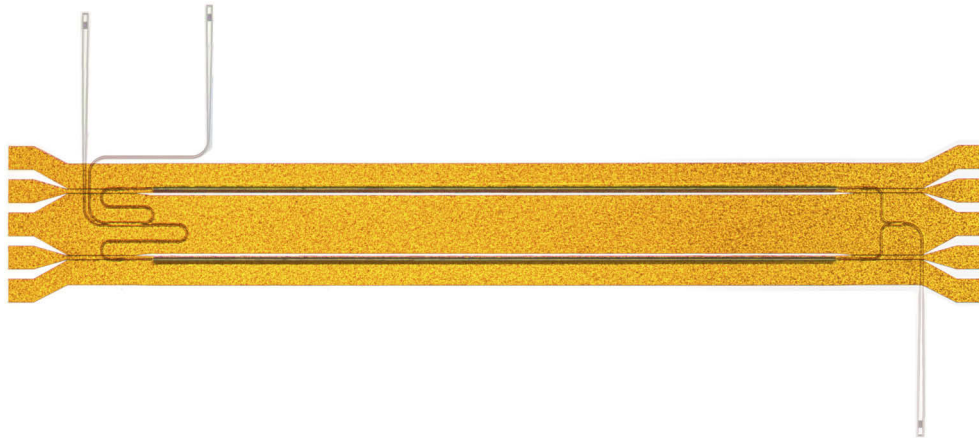


Fig. 4. Optical microscope image of the Mach-Zehnder modulator.

2.1. Mach-Zehnder Interferometer Modulator (MZM)

The Mach-Zehnder modulator (MZM) contains two 2 mm long arms each with the phase shifter shown in Fig. 2(a). A travelling wave electrode is used to ensure propagation of the RF and optical signals. The microwave effective refractive index is tuned to be 3.8 - 4.1 in the operating frequencies. The optical microscope image of the 2 mm long MZM is shown in Fig. 4.

The modulator is optimized solely for 2 μm operation, the MZM now includes gratings couplers and MMIs as opposed to previously demonstrated butt-coupling and Y-splitter approach [12]. The design parameters for the 1x2 and 2x2 MMI are listed in Table 1 and Fig. 5. In simulation, the insertion loss for each MMI is no bigger than 0.1 dB. The grating coupler is optimized for a 2 μm wavelength, the etch depth is 70 nm, the pitch of the gratings is 0.92 μm , the duty cycle is 0.552 (i.e. for each period silicon width is 0.508 μm and the air gap width is 0.412 μm) and the fully etched waveguide hosting the gratings is 10 μm in width. A taper with length of 500 μm tapers from the 10 μm wide grating region down to the width of the single mode strip waveguide, 550 nm. The multi mode region of the grating coupler is designed to have fully etched borders without slabs, the strip waveguide is used to bridge between the coupler and the rib waveguide in the active region. Also a relatively higher bend loss is experienced at a 2 μm wavelength than in C-band, the use of strip waveguides helps to keep the bend loss low. There is also a transition taper that gradually converts the strip access waveguide to a rib waveguide in the active region.

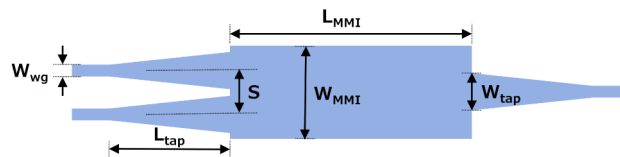


Fig. 5. Schematics diagram of MMI geometric parameters.

2.2. Michelson Interferometer Modulator (MIM)

The Michelson interferometer modulator resembles a MZM, but it uses reflectors to reflect light back from both arms, as shown in Fig. 6(a). Therefore, instead of combining and interfering the light from both arms at a second MMI, the Michelson interferometer uses the same MMI to split

Table 1. Design parameters for 2 μm wavelength 1x2 MMI Splitter and 2x2 MMI Coupler.

	1x2 MMI	2x2 MMI
Etch Depth	220 nm full etch	220 nm full etch
W_{wg}	0.55 μm	0.55 μm
W_{tap}	2.25 μm	2.25 μm
L_{tap}	10 μm	10 μm
W_{MMI}	6 μm	6 μm
L_{MMI}	23.44 μm	92.19 μm
S	3.25 μm	3.25 μm

the incident light and combine the reflected light. Thus light passes forth and back in total twice in the phase shifter which nearly doubles the efficiency of the modulator.

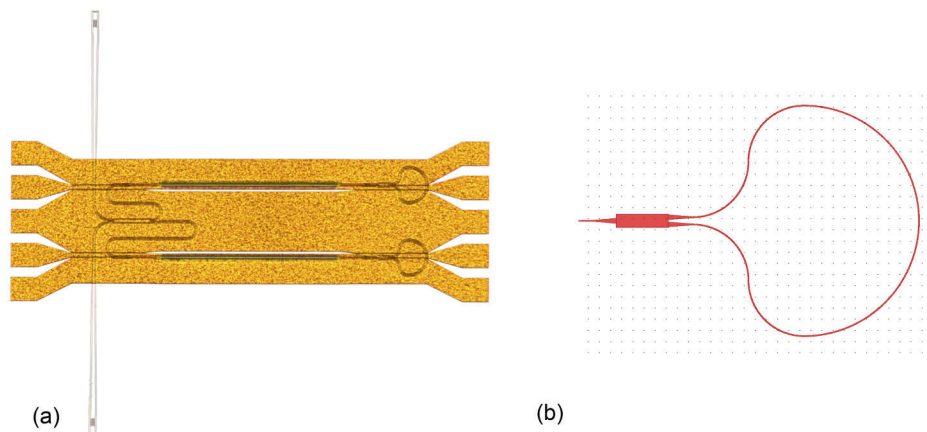


Fig. 6. (a) Optical microscope image of the Michelson interferometer modulator with loop mirror design. (b) Scanner mask layout for the looped mirror design in the Michelson interferometer.

In our design we used looped mirrors as reflectors as shown in Fig. 6(b). The looped mirror is advantageous in terms of reflectivity and ease of fabrication but introduces slightly larger optical delays compared to more compact mirrors such as metal reflectors or 1-D photonics crystal mirrors. The loop mirror consists of a 1x2 MMI with parameters from Table 1 and a section of waveguide arc. The total arc length is 319.26 μm .

The phase shifter length in the MIM is 0.5 mm. As a reference and for comparison, an MZM with the identical phase shifter design but twice the phase shifter length (1.0 mm) has been placed along side.

3. Experimental methodology

3.1. Experimental setup

Figure 7 shows a diagram of the experimental setup used during the DC and RF testing of the 2 μm modulators. A Thorlabs TLK-L1950R tunable laser is used as a seed of a bespoke TDFA. The TDFA is then pumped by an EDFA. Polarisation control is essential for the grating coupler, and for this we used a custom made fibre based polarisation controller made from SM2000 fibre with thin jacket and Thorlabs paddles. Light is coupled into and out of the Device Under Test

(DUT) with grating couplers. A Thorlabs low speed $2\ \mu\text{m}$ InGaAs detector with internal gain is used for fibre alignment and low speed characterisation. During the RF characterisation, an EOT ET-5000 high speed $2\ \mu\text{m}$ InGaAs detector is used. The detector has a rated bandwidth of $>12.5\ \text{GHz}$, and is the bottleneck in the high-speed link. For the electrical path, a pseudorandom binary sequence (PRBS) is outputted from an SHF 12104A Bit Pattern Generator (BPG) with a maximum 2 V peak-peak signal. In the push-pull configuration, no further RF amplifier is required. In the PAM-4 and MIM testing, a linear amplifier (SHF-S804A) is used to amplify the peak-peak voltage to 4V. The RF signal is combined with a DC bias in a bias Tee and is launched into the DUT via a ground-signal-ground-signal-ground (GSGSG) probe. External $50\ \Omega$ termination is applied to the output end of the modulator with another GSGSG probe.

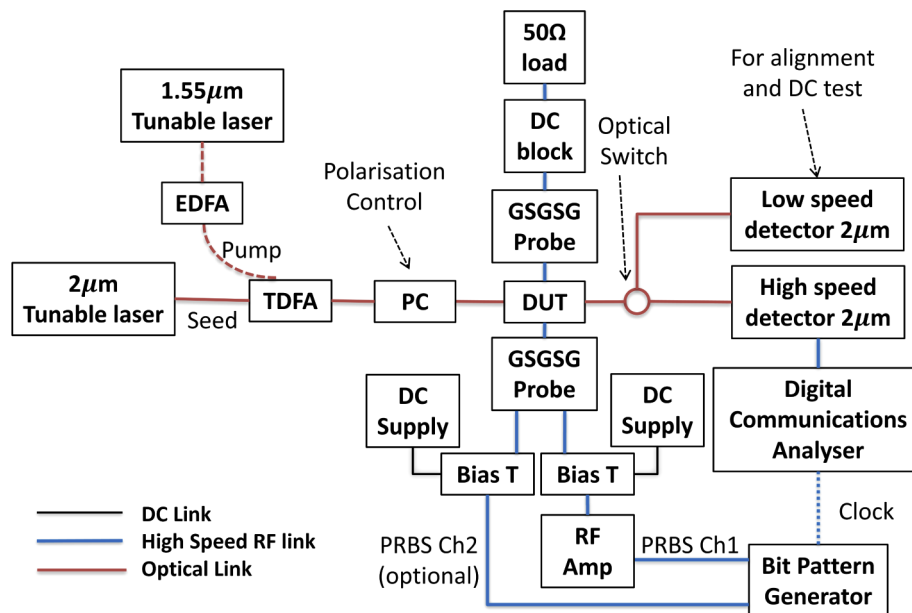


Fig. 7. High-speed RF measurement set up for $2\ \mu\text{m}$ wavelength modulator during PAM-4 characterisation.

3.2. Principle of streamlined PAM-4 operation

3.2.1. Existing optical PAM-4 modulation architectures with MZMs

There are mainly three methods to generate optical PAM-4 signal with MZMs.

Figure 8(a) illustrates a standard travelling wave MZM with a PAM-4 electrical drive signal. The electrical PAM-4 signal is generated by merging two electrical NRZ signals with an electrical digital-to-analogue converter (DAC). It is however difficult to design a high performance DAC, or for it to be cost effective in a product. Furthermore, the amplification of electrical PAM-4 signal requires dedicated highly-linear drive amplifier, which pose further challenge for high speed electrical devices. Lastly, in a single MZM, PAM-4 requires a higher optical extinction ratio (ER) and hence a longer device compared to OOK for a similar BER performance. The extended length may leads to adverse effects in the RF bandwidth.

The second option is to use a segmented MZM as shown in Fig. 8(b). Compared to the previous standard MZM, this shortens the arm length on each segment and helps maintain a high bandwidth. Both segments uses standard NRZ electrical driving signals, which involves no DAC and is therefore easier to generate. Nevertheless, the segmented design is inherently subject to

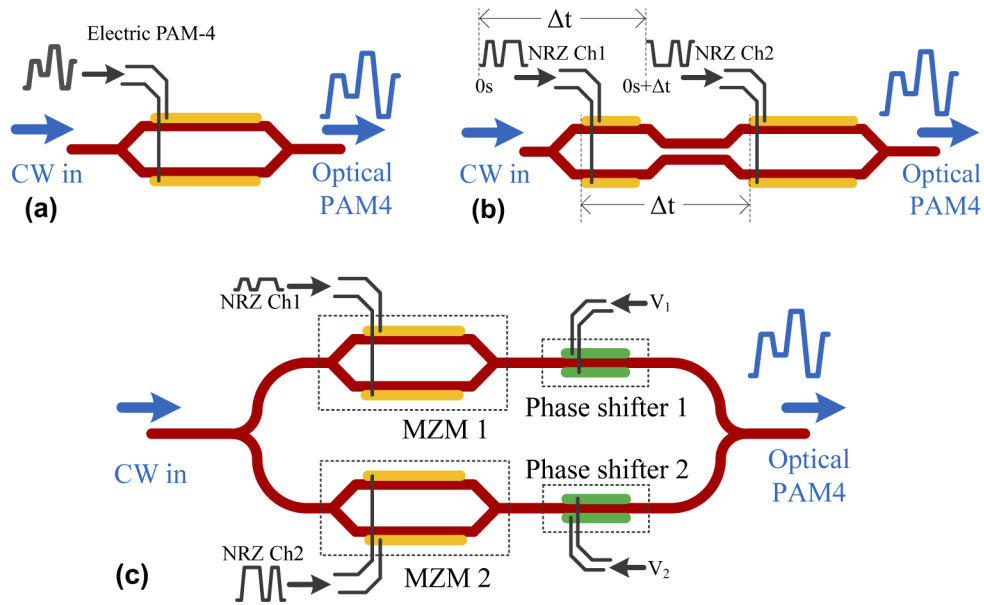


Fig. 8. (a) Conventional MZM with electronic DAC. (b) Segmented MZM with dual NRZ drive signal. (c) Parallel MZM with regulated dual NRZ drive signal. (d) Proposed streamlined PAM-4 modulation with dual-drive MZM. RV stands for reverse bias voltage. The upper arm NRZ 1 signal is been amplified to be 6 dB larger than the lower arm NRZ 2 signal. The more amplified drive signal carries the MSB and the other carries the LSB.

delay issue. The most significant bit (MSB) and least significant bit (LSB) driving signals need to be precisely tuned to offset the delay in the optical link. Controlling the delay in high data rate signals could be rather challenging to implement.

In Fig. 8(c) a pair of parallel MZMs are used to realise a PAM-4 transmitter. Both MZMs are identical in length, eliminating the delay issue. The MSB side then requires 6 dB more amplified NRZ signal than the LSB side. Extra phase shifters (often thermal) need to be added to fine tune the phase of the optical MSB signal and LSB signal so that they match each other. Since each modulator is only modulating half of the total input light, the driving peak-to-peak voltage would need to be higher than the segmented version to achieve the same ER.

3.2.2. Proposed streamlined IMDD PAM-4 with dual-drive MZM

We have proposed a streamlined method to implement the PAM-4 transmitter with a standard MZM. It needs only minimal modification of the current characterisation setup and without using an Arbitrary Waveform Generator (AWG). As illustrated in Fig. 9 the PAM-4 signal is generated by feeding NRZ electrical signals with different peak-to-peak power into each arm of the MZM. At the detection end, any phase information has been discarded and only intensity information is interpreted.

Here we analyse the system mathematically to prove the validity of the method. To simplify the calculation, zero optical loss has been assumed in each arm and the plasma dispersion effect induced loss has been neglected. The transfer function of a 1x1 MZI [19] can be simplified to

$$\frac{E_{OUT}}{E_{IN}} \approx \frac{1}{2} [e^{j(\omega t - \phi_1)} + e^{j(\omega t - \phi_2)}] \quad (1)$$

$$= e^{j\frac{\phi_1 + \phi_2}{2}} \cos\left(\frac{\phi_1 - \phi_2}{2}\right) \quad (2)$$

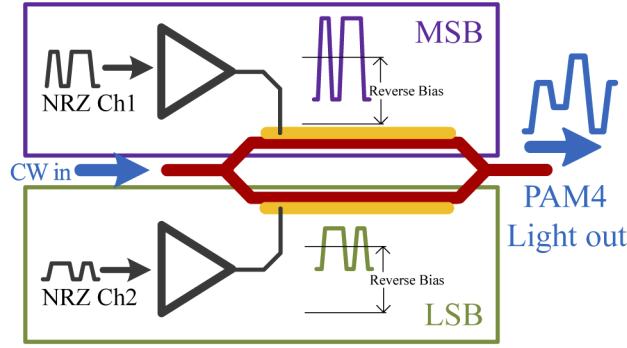


Fig. 9. Proposed streamlined PAM-4 modulation with dual-drive MZM. RV stands for reverse bias voltage. The upper arm NRZ 1 signal is been amplified to be 6 dB larger than the lower arm NRZ 2 signal. The more amplified drive signal carries the MSB and the other carries the LSB.

where E_{IN} is the optical input amplitude, E_{OUT} is the optical output amplitude, ϕ_1 and ϕ_2 are the phase delays induced in arm 1 and arm 2. The term $\frac{\phi_1 + \phi_2}{2}$ is the argument, which corresponds to the phase shift. And $|\cos(\frac{\phi_1 - \phi_2}{2})|$ is the magnitude, which corresponds to the amplitude change. In a MZM, the phase shift in each arm ϕ_i consists of inherent propagation delay ϕ'_i and phase shifter induced delay $\Delta\phi_i$. If we assume that the phase shifter response is linear, the phase change $\Delta\phi_i$ induced is linearly proportional to the reverse bias voltage V_i imposed.

$$\phi_1 = \phi'_1 + \Delta\phi_1 \approx \phi'_1 + \pi \frac{V_1}{V_\pi} \quad (3)$$

$$\phi_2 = \phi'_2 + \Delta\phi_2 \approx \phi'_2 + \pi \frac{V_2}{V_\pi} \quad (4)$$

When operating at the quadrature point, $\phi'_1 - \phi'_2 = \pi/2$. Therefore,

$$\frac{E_{OUT}}{E_{IN}} = \frac{1}{2} e^{j\left[\frac{\phi'_1 + \phi'_2}{2} + \frac{\pi}{2V_\pi}(V_1 + V_2)\right]} \cdot \cos\left[\frac{\phi'_1 - \phi'_2}{2} + \frac{\pi}{2V_\pi}(V_1 - V_2)\right] \quad (5)$$

$$= \frac{1}{2} e^{j\left[\frac{\phi'_1 + \phi'_2}{2} + \frac{\pi}{2V_\pi}(V_1 + V_2)\right]} \cdot \cos\left[\frac{\pi}{4} + \frac{\pi}{2V_\pi}(V_1 - V_2)\right] \quad (6)$$

The reverse bias voltages V_i each consists of a DC bias voltage V_{bias_i} and an RF AC signal with peak-to-peak voltage of V_{pp_i} .

$$V_1 = V_{bias_1} \pm \frac{V_{pp1}}{2} \quad (7)$$

$$V_2 = V_{bias_2} \pm \frac{V_{pp2}}{2} \quad (8)$$

If $V_{pp1} = 2V_{pp}$ and $V_{pp2} = V_{pp}$, $V_1 - V_2$ can then take these four distinctive levels.

$$V_1 - V_2 = \begin{cases} (V_{bias_1} - V_{bias_2}) + \frac{1}{2}(V_{pp1} + V_{pp2}) \\ (V_{bias_1} - V_{bias_2}) + \frac{1}{2}(V_{pp1} - V_{pp2}) \\ (V_{bias_1} - V_{bias_2}) + \frac{1}{2}(-V_{pp1} + V_{pp2}) \\ (V_{bias_1} - V_{bias_2}) + \frac{1}{2}(-V_{pp1} - V_{pp2}) \end{cases} \quad (9)$$

$$= \begin{cases} (V_{bias_1} - V_{bias_2}) + \frac{3}{2}V_{pp} \\ (V_{bias_1} - V_{bias_2}) + \frac{1}{2}V_{pp} \\ (V_{bias_1} - V_{bias_2}) - \frac{1}{2}V_{pp} \\ (V_{bias_1} - V_{bias_2}) - \frac{3}{2}V_{pp} \end{cases} \quad (10)$$

Since,

$$\frac{I_{OUT}}{I_{IN}} = \cos^2 \left[\frac{\pi}{4} + \frac{\pi}{2V_{\pi}}(V_1 - V_2) \right] \quad (11)$$

Therefore the output intensity of the MZM will also take four distinctive levels, if $\max(V_1 - V_2) < V_{\pi}/2$. The phase information is lost in the detection, and the whole system is effectively a intensity-modulation, direct detection (IMDD) PAM-4. However due to the residue phase in each output level, coherent application is not possible with this scheme. The linearity of PAM can be improved by choosing a RF driving signal with moderately small peak-to-peak voltage V_{pp} .

If $V_{pp1} = V_{pp}$ and $V_{pp2} = V_{pp}$, $V_1 - V_2$ can then take three distinctive levels.

$$V_1 - V_2 = \begin{cases} (V_{bias_1} - V_{bias_2}) + V_{pp} \\ (V_{bias_1} - V_{bias_2}) + 0 \\ (V_{bias_1} - V_{bias_2}) - V_{pp} \end{cases} \quad (12)$$

It is now a transmitter with a 3-level dual-binary signal output.

We have build a proof-of-principle simulation in Lumerical Interconnect to testify the proposed scheme. We fed two streams of 25 Gbit/s PRBS signals into each arm of a model MZM. The bias voltage is -2 V on both arms and the peak-to-peak voltages of the RF signal are 1 V and 2 V, corresponding to least significant bit (LSB) and most significant bit (MSB) respectively. A full coherent detector captures both phase and amplitude information and generates a constellation diagram. Figure 10 shows the heat map constellation diagram. It clearly shows four distinctive intensity modulation levels. The uneven spacing between levels are owing to non-linear response of the model modulator.

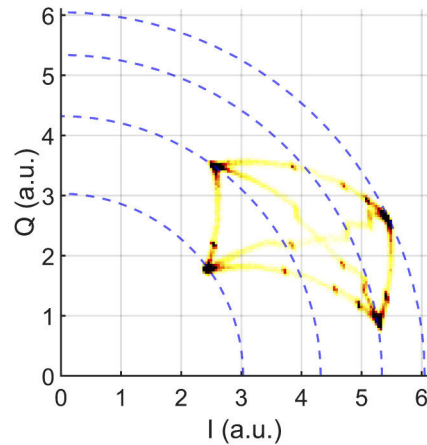


Fig. 10. Simulated the heat scatter constellation diagram of signal output from a streamlined PAM-4 transmitter, emphasizing the four intensity modulation states. I and Q both have arbitrary unit (A.U.).

4. Results and analysis

4.1. MZM OOK

The measured light intensity spectra under various bias DC voltages for the MZM that comprises a 2.0 mm long phase shifter is shown in Fig. 11(a). The phase shift for each DC voltages is extracted in Fig. 11(b). The single-arm modulation efficiency ($V_{\pi} \cdot L_{\pi}$) at a reverse bias of 4 V is 2.89 V·cm at 1950 nm.

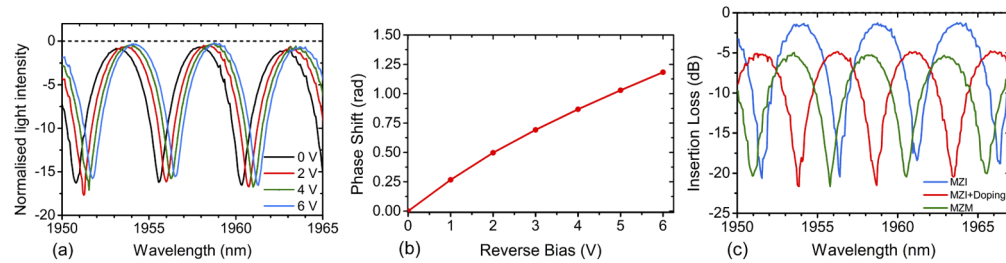


Fig. 11. (a) Normalised light intensity spectra from the MZM at 0–6 V reverse bias voltages. (b) Phase shift for a MZI modulator with 2 mm long phase shifter. (c) Insertion loss of the 2 mm MZM device and its two reference structures (MZM without metal electrode, MZI without metal nor doping).

The high-speed RF characterization is carried out in a push-pull configuration. The DC bias is -4.5 V. An high-speed $2^7 - 1$ pseudorandom-bit-stream OOK signal directly outputted from a BPG with a peak-to-peak amplitude of 2 V is applied on each arm. At wavelength of 1956.5 nm, the device modulates at 10 Gbit/s with an extinction ratio of 12.7 dB, as shown in Fig. 12(a), at 20 Gbit/s the extinction ratio is 10.3 dB, as in Fig. 12(b), and at 25 Gbit/s the extinction ratio is 6.25 dB, as in Fig. 12(c). Because of the bandwidth limit of the detector we were unable to obtain an open-eye diagram for data rates greater than 25 Gbit/s at a 2 μm wavelength.

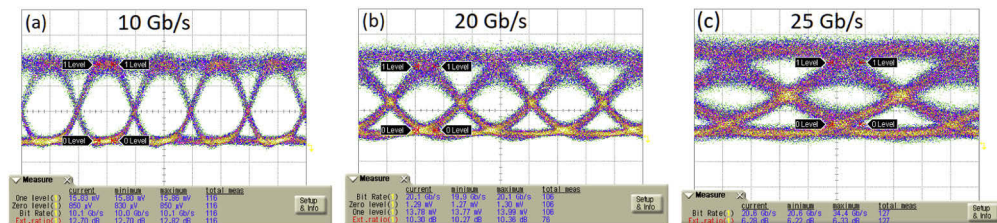


Fig. 12. Eye diagram for MZI modulator at 1956.5 nm wavelength. (a) Data rate 10 Gb/s, Extinction ratio 12.7 dB. (b) Data rate 20 Gb/s, extinction ratio 10.3 dB. (c) Data rate 25 Gb/s, extinction ratio 6.25 dB.

As indicated in Fig. 11(c), the insertion loss of the MZM with 2 mm phase shifters is 4.96 dB. A reference structure with all low dose and high dose doping but no metal is measured with an insertion loss of 4.76 dB. A third reference structure comprises only MZI without doping nor metal is shown to have a insertion loss of 1.25 dB. We could then deduce that doping accounts for a majority of the loss difference between MZM and MZI (around 3.51 dB), while metal electrodes only accounts for around 0.2 dB loss.

4.2. MZM PAM-4

The same MZM with 2 mm long phase shifters is used to perform the PAM-4 experiment. We have applied -4.5 V reverse bias on both arms. The LSB arm is fed with RF signal with

peak-to-peak voltage of 2 V directly outputted from the BPG. While for the MSB arm, the signal goes through a linear amplifier to provide a 4 V peak-to-peak signal. The two channels contain independent $2^7 - 1$ PRBS signals. This satisfies the PAM-4 condition in Eq. (10). RF-wise, the delays between the channels are adjusted in BPG to compensate for the propagation delay difference in the RF cables. The operation wavelength used is 1956.5 nm.

Figure 13(a) shows the eye diagram of a 20 Gbit/s PAM-4 signal (10 Gbaud), with an extinction ratio of $ER_{00-11} = 8.9$ dB. Figure 13(b) shows the eye diagram of a 25 Gbit/s PAM-4 signal (12.5 Gbaud/s), with an extinction ratio of $ER_{00-11} = 20$ dB. The high extinction ratio is due to the device not operating at the quadrature point. We have also tested the 30 Gbit/s PAM-4 signal as shown in Fig. 13(c) – the eye however is not open. This is likely caused by the noise from amplified spontaneous emission (ASE) introduced in the TDFA. The eye does not suffer from the nonlinear response as in Fig. 10. This is mainly because the peak to peak voltages (2 V and 4 V) are significantly smaller than the V_π (14.45 V for the 2 mm MZM driven by single arm), the modulation response is therefore mostly linear in this regime.

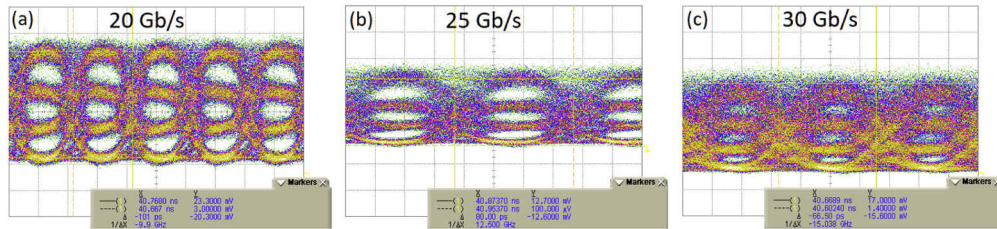


Fig. 13. Eye diagram showing PAM-4 operation of a 2 mm MZI modulator at a wavelength of 1950 nm. (a) 20 Gbit/s PAM-4. (b) 25 Gbit/s PAM-4. (c) 30 Gbit/s PAM-4.

4.3. MIM

The Michelson interferometer could produce significant back propagating light. Hence an optical isolator between the output TDFA and the device is essential to prevent any disturbance of the TDFA and the seed laser due to back reflections from the measured device.

In the DC regime, as shown in Fig. 14(a), the 0.5 mm long Michelson modulator has almost identical modulation efficiency to that of a 1 mm long MZM. They both have about half the efficiency of the 2 mm long MZM as expected. At a -4 V DC bias voltage, the 1 mm MZM has a measured modulation efficiency ($V_\pi \cdot L_\pi$) of 2.78 V·cm, whereas the Michelson interferometer modulator provides around double the performance due to its double pass, reaching 1.36 V·cm.

The measurement results obtained from loss analysis structures as given in Fig. 14(b) shows a similar result to the MZM case. The insertion loss of a Michelson interferometer modulator at zero bias is approximately 4.1 dB. The passive waveguide loss is ~2.45 dB, doping loss 1.1 dB and the metal and vias contribute to the remaining 0.55 dB loss.

For RF characterisation, only a single arm is driven. The $2^7 - 1$ pseudorandom-bit-stream OOK signal output from the BPG is amplified from 900 mV to 4 V peak-to-peak with an SHF S804A linear amplifier. The DC bias voltage is -2 V for the looped mirror Michelson modulator and -2.2 V for the MZM. To operate both devices at the quadrature point, a picked wavelength of 1954.10 nm is used for the Michelson modulator and 1955.10 nm for the MZM. The Michelson modulator with 0.5 mm long phase shifters gives an extinction ratio of 1.45 dB at 8 Gbit/s, and extinction ratio of 0.8 dB at 20 Gbit/s. The MZM with 1.0 mm phase shifters gives an extinction ratio of 1.98 dB at 8 Gbit/s, and extinction ratio of 1.97 dB at 20 Gbit/s. The eye diagrams of 0.5 mm MIM and 1.0 mm MZM are given in Fig. 15.

The degradation of the extinction ratio at 20 Gbit/s for the Michelson modulator is likely due to the mismatch of electrical and optical signal propagation. For moderately low data rates,

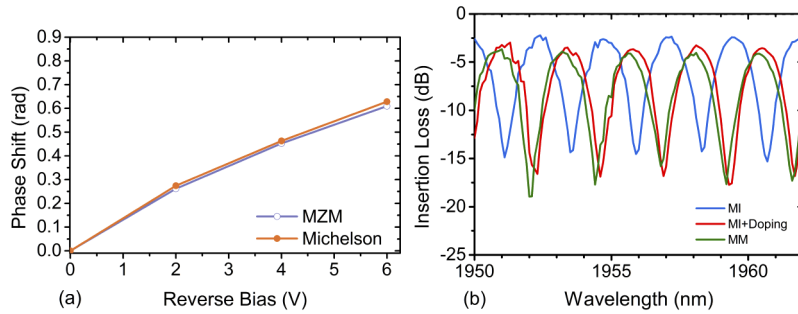


Fig. 14. (a) DC modulation efficiency of a looped-mirror Michelson interferometer modulator with 0.5 mm long phase shifter and a Mach-Zehnder interferometer modulator with 1.0 mm long phase shifter. (b) Insertion loss of the 0.5 mm Michelson interferometer modulator and its two reference structures (MIM without metal electrode, Michelson interferometer without metal nor doping).

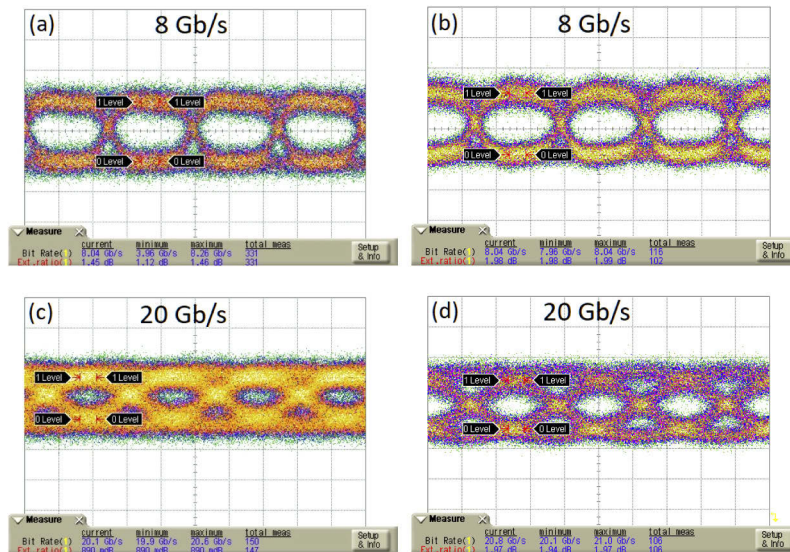


Fig. 15. Eye diagram for the 0.5 mm Michelson interferometer modulator and 1 mm MZI modulator at a wavelength of 1950 nm. (a) 0.5 mm MIM: Data rate 8 Gb/s, Extinction ratio 1.45 dB. (b) 1 mm MZM: Data rate 8 Gb/s, Extinction ratio is 1.98 dB. (c) 0.5 mm MIM: Data rate 20 Gb/s, Extinction ratio 0.89 dB. (d) 1 mm MZM: Data rate 20 Gb/s, Extinction ratio 1.97 dB.

MIM can be approximated as a lumped model and the degradation is minute; but at a data rate of 20 Gbit/s, the RF modulation efficiency drops significantly. This can be solved by adopting highly efficient modulation schemes and therefore significantly reducing the modulator length, for example accumulation type silicon modulators or Pockels effect modulators.

5. Conclusion

$2\mu\text{m}$ wavelength optimised carrier-depletion MZM and MIM have been designed, fabricated and characterised. The MZM with 2 mm long phase shifters operates at 25 Gbit/s OOK with an extinction ratio of 6.25 dB in a push-pull configuration. The insertion loss at zero bias is 4.96 dB and the single arm $V_{\pi} \cdot L_{\pi}$ efficiency is 2.89 V.cm at 4 V reverse bias. A streamlined

IMDD PAM-4 method has been proposed and mathematically analysed. The method is used to obtain 25 Gbit/s PAM-4 with the same MZM with 2mm long phase shifters. A Michelson interferometer modulator (MIM) with 0.5 mm long phase shifter length is demonstrated to have similar modulation strength to that of a MZM with 1.0 mm long phase shifter. The single arm $V_{\pi} \cdot L_{\pi}$ efficiency of the MIM is 1.36 V·cm at 4 V reverse bias. Both MIM with 0.5 mm long phase shifters and MZM with 1 mm long phase shifters operate at 20 Gbit/s OOK with single arm driving.

Supplemental Documents

Data supporting this study are openly available in [Dataset 1 \[20\]](https://doi.org/10.5258/SOTON/D1685) from the University of Southampton repository at <https://doi.org/10.5258/SOTON/D1685>

Funding. Royal Academy of Engineering (RF201617/16/33); Royal Society (UF150325); Engineering and Physical Sciences Research Council (EP/L021129/1, EP/N00762X/1, EP/R003076/1).

Disclosures. The authors declare no conflicts of interest.

References

1. D. J. Richardson, "Filling the light pipe," *Science* **330**(6002), 327–328 (2010).
2. A. Ellis, J. Zhao, and D. Cotter, "Approaching the non-linear shannon limit," *J. Lightwave Technol.* **28**(4), 423–433 (2010).
3. R.-J. Essiambre, G. Kramer, P. J. Winzer, G. J. Foschini, and B. Goebel, "Capacity limits of optical fiber networks," *J. Lightwave Technol.* **28**(4), 662–701 (2010).
4. P. J. Roberts, F. Couny, H. Sabert, B. J. Mangan, D. P. Williams, L. Farr, M. W. Mason, A. Tomlinson, T. A. Birks, J. C. Knight, and P. S. J. Russell, "Ultimate low loss of hollow-core photonic crystal fibres," *Opt. Express* **13**(1), 236 (2005).
5. E. Desurvire, C. Kazmierski, F. Lelarge, X. Marcadet, A. Scavennec, F. Kish, D. Welch, R. Nagarajan, C. Joyner, R. Schneider, S. Corzine, M. Kato, P. Evans, M. Ziari, A. Dentai, J. Pleumeekers, R. Muthiah, S. Bigo, M. Nakazawa, D. Richardson, F. Poletti, M. Petrovich, S. Alam, W. Loh, and D. Payne, "Science and technology challenges in XXIst century optical communications," *C. R. Phys.* **12**(4), 387–416 (2011).
6. F. Poletti, N. V. Wheeler, M. N. Petrovich, N. Baddela, E. N. Fokoua, J. R. Hayes, D. R. Gray, Z. Li, R. Slavik, and D. J. Richardson, "Towards high-capacity fibre-optic communications at the speed of light in vacuum," *Nat. Photonics* **7**(4), 279–284 (2013).
7. P. J. Roberts, "Control of dispersion in hollow core photonic crystal fibers," in *2007 Conference on Lasers and Electro-Optics (CLEO)*, (IEEE, 2007).
8. R. Slavik, G. Marra, E. N. Fokoua, N. Baddela, N. V. Wheeler, M. Petrovich, F. Poletti, and D. J. Richardson, "Ultralow thermal sensitivity of phase and propagation delay in hollow core optical fibres," *Sci. Rep.* **5**(1), 15447 (2015).
9. L. Olanterae, C. Sigaud, J. Troska, F. Vasey, M. N. Petrovich, F. Poletti, N. V. Wheeler, J. P. Wooler, and D. J. Richardson, "Gamma irradiation of minimal latency hollow-core photonic bandgap fibres," *J. Instrum.* **8**(12), C12010 (2013).
10. J. J. Ackert, D. J. Thomson, L. Shen, A. C. Peacock, P. E. Jessop, G. T. Reed, G. Z. Mashanovich, and A. P. Knights, "High-speed detection at two micrometres with monolithic silicon photodiodes," *Nat. Photonics* **9**(6), 393–396 (2015).
11. W. Wang, Z. Zhang, X. Guo, J. Zhou, S. J. X. Brian, M. S. Rouifed, C. Liu, C. Littlejohns, G. T. Reed, and H. Wang, "Mid-infrared (MIR) mach-zehnder silicon modulator at 2 μ m wavelength based on interleaved PN junction," in *Conference on Lasers and Electro-Optics*, (OSA, 2018).
12. W. Cao, D. Hagan, D. J. Thomson, M. Nedeljkovic, C. G. Littlejohns, A. Knights, S.-U. Alam, J. Wang, F. Gardes, W. Zhang, S. Liu, K. Li, M. S. Rouifed, G. Xin, W. Wang, H. Wang, G. T. Reed, and G. Z. Mashanovich, "High-speed silicon modulators for the 2 μ m wavelength band," *Optica* **5**(9), 1055 (2018).
13. W. Li, M. Li, H. Zhang, Y. Zhang, H. Xie, X. Xiao, and K. Xu, "50 Gbit/s silicon modulator operated at 1950 nm," in *Optical Fiber Communication Conference (OFC) 2020*, (OSA, 2020).
14. D. E. Hagan, M. Ye, P. Wang, J. C. Cartledge, and A. P. Knights, "High-speed performance of a TDFA-band micro-ring resonator modulator and detector," *Opt. Express* **28**(11), 16845 (2020).
15. M. Nedeljkovic, R. Soref, and G. Z. Mashanovich, "Free-carrier electrorefraction and electroabsorption modulation predictions for silicon over the 1-14- μ m infrared wavelength range," *IEEE Photonics J.* **3**(6), 1171–1180 (2011).
16. A. B. Fallahkhair, K. S. Li, and T. E. Murphy, "Vector finite difference modesolver for anisotropic dielectric waveguides," *J. Lightwave Technol.* **26**(11), 1423–1431 (2008).
17. C. G. Littlejohns, D. J. Rowe, H. Du, K. Li, W. Zhang, W. Cao, T. D. Bucio, X. Yan, M. Banakar, D. Tran, S. Liu, F. Meng, B. Chen, Y. Qi, X. Chen, M. Nedeljkovic, L. Mastronardi, R. Maharjan, S. Bohora, A. Dhakal, I. Crowe, A. Khurana, K. C. Balram, L. Zagaglia, F. Floris, P. O'Brien, E. D. Gaetano, H. M. Chong, F. Y. Gardes, D. J. Thomson,

- G. Z. Mashanovich, M. Sorel, and G. T. Reed, "CORNERSTONE's silicon photonics rapid prototyping platforms: Current status and future outlook," *Appl. Sci.* **10**(22), 8201 (2020).
18. D. J. Thomson, F. Y. Gardes, S. Liu, H. Porte, L. Zimmermann, J.-M. Fedeli, Y. Hu, M. Nedeljkovic, X. Yang, P. Petropoulos, and G. Z. Mashanovich, "High performance mach-zehnder-based silicon optical modulators," *IEEE J. Sel. Top. Quantum Electron.* **19**(6), 85–94 (2013).
19. G. T. Reed ed., *Silicon Photonics: The State of the Art* (John Wiley & Sons, Ltd, 2008), pp. 247–248.
20. W. Cao, S. Liu, C. G. Littlejohns, D. J. Thomson, M. Nedeljkovic, W. Zhang, K. Li, M. Banakar, Y. Tran, X. Yan, H. Du, Z. Ren, F. Gardes, G. T. Reed, and G. Z. Mashanovich, "Dataset for High-speed silicon Michelson interferometer modulator and streamlined IMDD PAM-4 transmission of Mach-Zehnder modulators for the 2 μm wavelength band," figshare 2021 <https://doi.org/10.6084/m9.figshare.13483125>.